TISSUE ENGINEERING: Part C
Volume 18, Number 9, 2012

DOI: 10.1089/ten.tec.2011.0744

Longitudinal *In Vivo* Imaging to Assess Blood Flow and Oxygenation in Implantable Engineered Tissues

Sean M. White, M.S.,[1,2] Ryan Hingorani,[1,*] Rajan P.S. Arora, B.S.,[1,*] Christopher C.W. Hughes, Ph.D.,[1,3,4] Steven C. George, M.D., Ph.D.,[1,3,5,*] and Bernard Choi, Ph.D.[1–3,*]

The functionality of vascular networks within implanted prevascularized tissues is difficult to assess using traditional analysis techniques, such as histology. This is largely due to the inability to visualize hemodynamics *in vivo* longitudinally. Therefore, we have developed dynamic imaging methods to measure blood flow and hemoglobin oxygen saturation in implanted prevascularized tissues noninvasively and longitudinally. Using laser speckle imaging, multispectral imaging, and intravital microscopy, we demonstrate that fibrin-based tissue implants anastomose with the host (severe combined immunodeficient mice) in as short as 20 h. Anastomosis results in initial perfusion with highly oxygenated blood, and an increase in average hemoglobin oxygenation of 53%. However, shear rates in the preformed vessels were low ($20.8 \pm 12.8\,s^{-1}$), and flow did not persist in the vast majority of preformed vessels due to thrombus formation. These findings suggest that designing an appropriate vascular network structure in prevascularized tissues to maintain shear rates above the threshold for thrombosis may be necessary to maintain flow following implantation. We conclude that wide-field and microscopic functional imaging can dynamically assess blood flow and oxygenation *in vivo* in prevascularized tissues, and can be used to rapidly evaluate and improve prevascularization strategies.

Introduction

Tissue engineering offers numerous possibilities to repair or replace diseased and damaged tissue. However, a primary obstacle hampering the creation of clinically relevant thick engineered tissue is the adequate transport of nutrients and waste. For the majority of tissues, the rate-limiting nutrient is oxygen, which has a diffusion limit of ~100–200 μm[1–3] in metabolically active tissues (e.g., cardiac muscle). As a result, any densely cellularized engineered tissue with a dimension >200 μm will require the rapid development of a functional vessel network upon implantation. Difficulties in creating such vessel networks have limited clinically applicable engineered tissues to thin avascular tissues, such as skin and cartilage.[4–8]

Several strategies have been developed to enhance vascularization of engineered tissue implants. These strategies include utilizing cellular scaffolds that facilitate convective flow and host vessel infiltration,[9] including angiogenic growth factors, such as vascular endothelial growth factor to encourage host vessel infiltration,[10] cellularizing previously vascularized decellularized tissues,[11,12] and prevascularizing implants both *in vivo* and *in vitro*.[13–16] Manipulation of scaffold design and inclusion of angiogenic growth factors both rely on host vessel infiltration, which may be too slow to maintain viability in thick engineered tissues.[17,18] Use of decellularized matrices is promising due to the presence of a pre-existing matrix and its associated cellular cues. However, recellularization and restoration of tissue function remain significant hurdles.

We previously demonstrated the potential of *in vitro* prevascularization by seeding fibrin-based tissues with endothelial colony-forming cell-derived endothelial cells (ECFC-ECs) and normal human lung fibroblasts (NHLFs). An extensive network of microvessels develops *in vitro* over the ensuing week. Upon implantation into severe combined immunodeficient (SCID) mice, the human vessels anastomose with the host vasculature resulting in implant perfusion in as short as 27 h.[16]

Although studies such as these constitute marked progress toward maintaining implant viability in thicker and more clinically relevant engineered tissues, assessing the function of the vessel network has been largely limited to postsacrifice histology.[15,16,19–23] Histology cannot assess the dynamics of perfusion, blood oxygenation, vascular organization, vessel remodeling, or cell viability. Further, histological processing

[1]Department of Biomedical Engineering, [2]Beckman Laser Institute and Medical Clinic, [3]Edwards Lifesciences Center for Advanced Cardiovascular Technology, [4]Department of Molecular Biology and Biochemistry, and [5]Department of Chemical Engineering and Material Science, University of California, Irvine, California.
*These authors contributed equally to this work.

is destructive, and can introduce potential artifacts that confound physiological interpretation. We have therefore implemented intravital functional imaging techniques to longitudinally analyze prevascularized tissues following *in vivo* implantation into the dorsal window chamber of SCID mice. These techniques include intravital microscopy, multispectral imaging (MSI), and laser speckle imaging (LSI). Intravital imaging of implanted cells or tissue using microscopy and MSI has been established previously in the literature to longitudinally analyze the morphology and flow within blood vessels, as well as acquire blood oxygen saturation information in dorsal window chambers.[13,24–26] Alternatively, LSI has been used to create flow maps in small rodents[27–30]; however, it has not been used to study blood flow in prevascularized implants. Our methodology thus allows assessment of oxygenation, vascular morphology, and blood flow dynamically, and can therefore ameliorate the development of prevascularized implantable tissues.

Materials and Methods

ECFC-EC isolation

ECFC-ECs were isolated from human umbilical cord blood that was obtained from the University of California Irvine Medical Center according to an Institutional Review Board–approved protocol. ECFC-EC isolation was performed as follows.[16] Mononuclear cells were separated from 15 to 20 mL cord blood using a lymphocyte separation medium (Fisher Scientific, Pittsburgh, PA). The mononuclear cells were then seeded on 1% gelatin (Sigma-Aldrich, St. Louis, MO)–coated tissue culture flasks and fed with a 1:1 mixture of endothelial growth medium (EGM-2; Lonza, Walkersville, MD) and M199 (Invitrogen, Carlsbad, CA), supplemented with 20% fetal bovine serum and 1% endothelial cell growth supplements (Fisher Scientific) for 2–4 weeks. The endothelial outgrowth cells were purified using CD-31 (Dako, Carpinteria, CA)–coated magnetic beads (New England Biolabs, Ipswich, MA).

Creation of prevascularized tissues

Prevascularized tissues ($n=12$) were composed of ECFC-ECs and NHLFs suspended in a fibrin matrix. Prior to tissue preparation, ECFC-ECs and NHLFs were cultured in EGM-2 (Lonza) and fibroblast growth medium, respectively (Lonza). Media were changed every 2–3 days. ECFC-ECs were used from passages 3–5 and NHLFs were used from passages 3–6. During tissue preparation, cells were trypsinized and resuspended in 10 mg/mL bovine fibrinogen (Sigma-Aldrich) dissolved in serum and phenol red free Dulbecco's modified Eagle's medium (DMEM; Invitrogen) to a final concentration of 1×10^6 ECFC-ECs/mL and 2×10^6 NHLFs/mL. These cellular concentrations have been previously shown to result in *in vitro* vessel formation and *in vivo* perfusion following implantation.[16] Fifty microliters of cell suspension was pipetted onto a 12-mm circular glass cover slip with an affixed polydimethylsiloxane (PDMS)–retaining ring (Fig. 1, inset) and mixed with 4 μL of 50 units/mL bovine thrombin (Sigma-Aldrich). The PDMS-retaining rings had a diameter of 8 mm and a height of 0.8 mm. Tissues were allowed to polymerize for 20 min at 37°C and were then suspended in EGM-2 and maintained at 37°C in 100% humidified air containing 5% CO_2 for the next 7 days. Control tissues ($n=5$) were created using the same steps but without the addition of cells. The final thickness of the implantable tissues was ~1 mm. Media were changed every 2–3 days.

Staining of ECFC-ECs with DiO

ECFC-ECs to be stained with DiO prior to implantation were first trypsinized and centrifuged at 1000 rpm for 5 min. The cell pellet was resuspended in serum and phenol red free DMEM (Invitrogen) to a concentration of 1×10^6 cells/mL. Ten microliters of DiO (Invitrogen) per milliliter of cell suspension was added, and the mixture was incubated at 37°C for 20 min. The cell suspension was then centrifuged at 1000 rpm for 5 min, and the cell pellet was resuspended in 10 mg/mL bovine fibrinogen dissolved in serum and phenol red free DMEM (Invitrogen). NHLFs were then added to the fibrinogen solution such that the final concentration of cells was 1×10^6 ECFC-ECs/mL and 2×10^6 NHLFs/mL. The aforementioned methods for creating prevascularized tissues were then followed.

In vitro *quantification of blood vessel diameter, vessel length, and bifurcation density in prevascularized tissues*

Three prevascularized tissues were created as described previously but were used for *in vitro* image analysis rather than implantation. Following 7 days of incubation, tissues were fixed in 10% formalin and vessels were stained using a mouse anti-human antibody to CD-31 (Dako) as described previously and as follows.[16] Tissues were blocked with a 2% bovine serum albumin (Sigma-Aldrich) and 0.1% Tween 20 (Sigma-Aldrich) solution for 2 h, followed by incubation overnight with the primary antibody, diluted 1:200 in a 0.1% Tween 20 solution. They were then washed four times for 1 h, followed by incubation overnight with an Alexa Fluor 488–labeled goat anti-mouse antibody (Invitrogen), diluted 1:500 in a 0.1% Tween 20 solution. Tissues were washed four times for 1 h prior to imaging. Ten separate areas in each tissue were imaged at 100× magnification. Vessel diameter was computed manually at points equidistant from vessel nodes. Vessel length was also computed manually between vessel nodes. The number of vessel bifurcations was computed automatically using a custom-written program developed in the MATLAB programming environment (MathWorks, Natick, MA). This program searches for and enumerates bifurcations of predefined shape in vessel images following skeletonization (see MATLAB m-files in Supplementary Data [available online at www.liebertonline.com/tec]).

Animal model

All *in vivo* experiments were conducted under a protocol approved by the Institutional Animal Care and Use Committee at the University of California, Irvine. Titanium dorsal window chambers were surgically installed onto the dorsal area of ICR-SCID (Taconic Farms, Oxnard, CA) mice ($n=17$) under anesthesia (50 mg/kg ketamine and 5 mg/kg xylazine administered via i.p. injection). Additional anesthetics were administered during surgery as needed. Installation was performed as follows.[31,32] Animals' eyes were first lubricated with a sterile ophthalmic ointment to prevent corneal

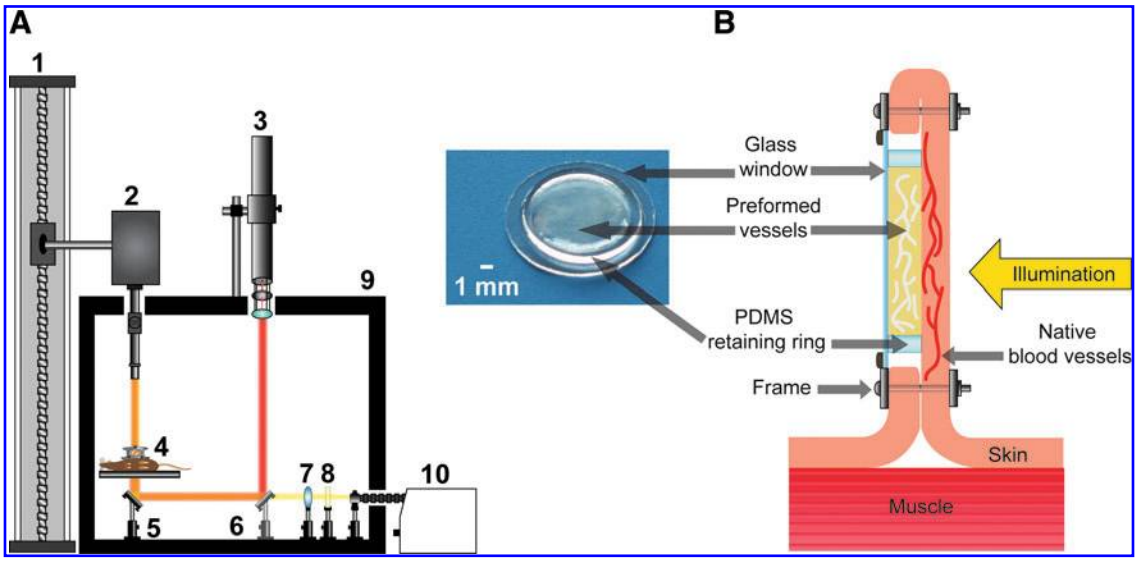

FIG. 1. **(A)** Multimodal imaging platform used to perform laser speckle imaging (LSI) and multispectral imaging (MSI). (1) Motorized slide for large height adjustment of multispectral camera. (2) Multispectral camera with variable magnification lens system and liquid crystal tunable filter that can be removed from the beam path. (3) Helium-neon laser with attached polarizer for intensity attenuation and beam expansion optics used for transillumination during LSI. (4) Mouse bearing dorsal window chamber resting upon circulating water heating block. (5) Mirror at 45° used to redirect light through dorsal window chamber for transillumination. (6) Removable mirror at 45° to redirect laser light for transillumination during LSI. (7) Collimation optics for quartz halogen lamp. (8) Infrared filter. (9) Light-tight enclosure. (10) 150 W quartz halogen lamp. **(B)** Magnified view of (4) showing mouse dorsal window chamber in cross-section, orientation of implanted prevascularized tissue, and direction of illumination. Inset photograph is a prevascularized tissue, shown with the polydimethylsiloxane (PDMS) ring and 12-mm cover slip present during *in vitro* culture and implantation into the dorsal window chamber. Color images available online at www.liebertonline.com/tec

dehydration. Dorsal hair was removed using electric clippers, followed by application of a commercial depilatory cream (Nair; Church & Dwight Co., Inc., Princeton, NJ) to remove fine hair.

The dorsal skin was then pulled up and transilluminated using a white light source to enable visualization of the surgical field and location of blood vessels. One half of the window chamber frame was used as a template to find the appropriate placement. Three 16-gauge needles were pushed through the bolt holes of the window chamber frame and underlying dorsal skin, creating a channel through which bolts could be pushed. The needles were then removed and bolts were pushed through the three bolt holes of the window chamber frame. Spacers were threaded onto each of the three bolts and the remaining half of the window chamber frame was placed over the points of the inserted bolts. The window chamber assembly was then secured by screwing three nuts onto the frame bolts, followed by suturing the frame and dorsal skin together via suture holes at the four corners of the window chamber frame.

The skin framed by the window chamber was then pinched upward using forceps and a roughly 1-mm-long incision was made into the skin. This incision was used to remove one full thickness of skin, revealing the dermis of the underlying skin. A small ($\sim$0.5 mm) border of skin around the frame opening was left to prevent the leakage of fluid from the window chamber. Fine-tipped forceps and microscissors were then used to remove fascia from the exposed skin. Approximately 100 μL of sterile saline was injected into the window chamber to avoid air bubbles, and the window chamber was closed by placing the cover slip on which a prevascularized tissue was cultured into the window of the frame, placing the tissue in direct contact with the dermis of the exposed skin. Mice were imaged once per day for 7 days, followed by once every 7 days for 2 weeks thereafter. After all imaging was completed, mice were sacrificed via pentobarbital overdose.

Imaging systems

LSI and MSI were performed on the implanted tissues at magnifications from 0.5× to 250× as shown in Figure 1 and as described previously.[33] Briefly, two illumination sources were used for imaging, a 150 W quartz halogen lamp (Edmund Optics, Barrington, NJ) during MSI, and a 30 mW 633 nm helium-neon laser (Newport, Irvine, CA) during LSI. During MSI, light from the quartz halogen lamp was directed through an infrared filter to prevent heating the dorsal window chamber, followed by a plano-convex lens for spatial collimation. A mirror was then used to redirect the light such that it transilluminated the dorsal window chamber and entered the detection optics. During LSI, the helium-neon laser beam was first directed through a rotatable linear polarizer that was used to control the light intensity. The beam was then directed through a beam expander (Newport) and toward the dorsal window chamber using one removable and one stationary mirror. The beam spot size was $\sim$2 cm upon transilluminating the dorsal window chamber. Detection was performed using a charge-coupled device (CCD) camera with a removable liquid crystal tunable filter with a bandwidth of 400–720 nm (Nuance; Caliper Life Sciences, Woburn, MA), which could be moved up and

down using a motorized slide to accommodate usage of optics with varying working distances. During LSI and MSI, mice were anesthetized under 1.5% isoflurane with balance oxygen and placed on a circulating water heating block. All color images shown are composites of MSI cubes acquired from 420 to 720 nm in 20-nm steps. Fluorescence microscopy (Nikon TE800 and Diaphot TMD; Nikon, Melville, NY) was also performed. In some experiments, the mouse vasculature was imaged following retro-orbital injection of 150 kDa fluorescein isothiocyanate (FITC)–dextran (Sigma-Aldrich) at a concentration of 10 mg/mL in saline. Following injection of FITC-dextran, imaging was performed at 30 frames per second.

Laser speckle imaging

LSI was used to create maps of the relative flow of blood in and around implanted tissues.[27,28,34] To assure that preformed vessels smaller than 20 μm (the approximate spatial resolution of the imaging system at 1×) were resolved using LSI, all imaging was performed at magnifications of 1× and above. During LSI, the dorsal window chamber was transilluminated using a helium-neon laser and 10 images were acquired at three camera exposure times (T): 10, 100, and 1000 ms. Multiple exposure times were used to compensate for the fact that the linearity and sensitivity of LSI depends on proper choice of exposure time in relation to the speed of blood movement within an image.[27,29,35,36] Use of longer exposure times increases sensitivity to the relatively slow flow in small-caliber vessels.[33,36] One thousand millisecond exposure times are capable of detecting flow speeds as slow as 15 μm/s (unpublished data). Laser intensity was adjusted for each exposure time using a polarizer such that the entire dynamic range of the CCD camera was utilized without overexposure. Speckle contrast images were then computed from the collected raw images by performing the following computation using a 7×7 sliding window algorithm:

$$K = \frac{\sigma}{<I>} \tag{1}$$

where K is speckle contrast, σ is the standard deviation of the pixel values within the sliding window, and $<I>$ is the average intensity of the pixel values within the sliding window. Care was taken to assure that, on average, each imaged speckle was sampled by at least two CCD pixels to satisfy the Nyquist criterion.[37] The 10 speckle contrast images computed for each exposure time were then averaged together to reduce noise and the resultant image was used to compute a speckle flow index (SFI) map using the following simplified speckle imaging equation at each pixel:

$$SFI = \frac{1}{2TK^2} \tag{2}$$

SFI is assumed to be inversely proportional to the correlation time at each pixel and thus proportional to the speed of blood flow.[30,38] All image processing was performed using MATLAB (m-files available in Supplementary Data).

Generation of hemoglobin absorption maps

MSI data collected from 500 to 580 nm in 5-nm steps were used to create maps of hemoglobin absorption. The absorption at each of the 17 collected wavelengths was computed for 10 pixels corresponding to one arteriole and 10 pixels corresponding to one venule as determined by morphological features and hemoglobin oxygen saturation (SO_2) map analysis. These 20 absorption spectra were then averaged together. The absorption spectrum at each pixel was then compared with the resulting absorption spectrum via calculation of the correlation coefficient. The resulting map of correlation coefficients was then normalized to one. Image processing was performed using Nuance (Caliper Life Sciences) and MATLAB.

Calculation of shear rates in preformed and native vessels

Shear rates within blood vessels were calculated from videos of erythrocyte movement acquired using intravital fluorescence microscopy following FITC-dextran injection. The shear rate at the vessel wall (where it is the largest) was approximated as

$$\dot{\gamma} = \frac{4v}{r} \tag{3}$$

where $\dot{\gamma}$ is shear rate (s^{-1}), v is average cross-sectional fluid speed (μm/s), and r is blood vessel radius (μm). Average fluid speed was estimated by dividing the distance traveled by imaged erythrocytes over a given time period, and r was measured in the center of the vessel through which the erythrocyte was traveling. Measurements were performed on vessel locations that were free of significant bending and changes in diameter.

Calculation of vascular density and functional vascular density

Vascular density (VD) (length of blood-filled vessels not necessarily exhibiting flow per unit area) and functional vascular density (FVD) (length of vessels exhibiting flow per unit area) were computed using custom-written software.[36] VD was computed using the hemoglobin absorption maps, as they offer high contrast between blood vessels and background and do not rely on flow for inclusion in the computation. FVD was computed using SFI maps acquired using a 1000-ms exposure. This allowed only vessels containing flowing blood to contribute to the computation. To compute FVD or VD in each image, processing was performed as follows. Vessel edges in each image were first accentuated by using a low-pass filter and the resultant image was subtracted from the original image. The result was then thresholded for intensity and object size to isolate vessels and remove noise. A median filter to smooth vessel edges was then applied to the binary image. The resulting image was then skeletonized so that all objects were reduced to one pixel in diameter along the medial axis, and FVD or VD was computed by summing the length of all vessels divided by the area of the region of interest. VD and FVD values for each subject were normalized by dividing computed VD and FVD values by their respective values on day 1 of imaging.

Creation of hemoglobin oxygen saturation maps

MSI was used to create hemoglobin SO_2 maps, which has been described in detail elsewhere and briefly as

follows.[25,32,39] During MSI, the window chamber was transilluminated using a halogen lamp. Seventeen images from 500 to 580 nm in 5-nm increments were acquired using the multispectral camera with the liquid crystal tunable filter in the light path. The exposure time at each image was adjusted such that the entire dynamic range of the CCD camera was utilized without overexposure. Hemoglobin oxygen saturation was computed using the following model equation based upon the Beer-Lambert equation:

$$\log\left(\frac{I_0}{I}\right) = OD(\lambda) = \varepsilon_{HbO_2}(\lambda)[HbO_2]L(\lambda) + \varepsilon_{Hb}(\lambda)[Hb]L(\lambda) + S(\lambda)L(\lambda) \quad (4)$$

where λ is wavelength; I is the detected light intensity at a given pixel; I_0 is the incoming light intensity; OD is optical density; ε_{HbO2} and ε_{Hb} are the extinction coefficients of oxyhemoglobin and deoxyhemoglobin, respectively; $[HbO_2]$ and $[Hb]$ are the concentration of oxyhemoglobin and deoxyhemoglobin, respectively; L is the path length traveled by the sampled light; and S is a scattering term meant to compensate for incoming light that is scattered rather than absorbed at an area of interest.

Images were converted to optical density by choosing an I_0 value from an apparently avascular region. Using ε_{HbO2} and ε_{Hb} values acquired with our imaging system, hemoglobin saturation was computed using linear least-squares regression at each pixel. Pixel fits with an $R^2 < 0.95$ were set to zero. The wavelength dependence of S and L was ignored for simplicity. However, assuming no wavelength dependence for S has been shown to produce more accurate results than using a more complicated dependence such as $\lambda^{-1.7}$.[25,40] The value for S was determined by allowing mice to breathe 1.5% isoflurane mixed with 98.5% oxygen, imaging the window chamber using SO_2 mapping, and calculating a value of S that would result in a computed hemoglobin oxygenation of 98% within an arteriole. Arterioles were identified via morphology and hemoglobin saturation values >95% in SO_2 maps taken prior to correction. All image processing was performed using MATLAB.

Average hemoglobin oxygenation was computed in the entire window for each subject at every time point. These values were then divided by the corresponding VD values from the same time point to compensate for differences in the number of vessels contributing to the average hemoglobin oxygenation. Dividing the SO_2 values by the corresponding value from day 1 then normalized the resultant values.

Histology

Following host sacrifice, implanted tissues were removed with adjacent host skin and fixed in 10% formalin. Samples were embedded in paraffin and sectioned in the coronal plane into slices 4 μm in thickness. Sections were alternately stained with hematoxylin and eosin or immunofluorescently labeled using an anti-human CD-31 antibody (Dako). Immunofluorescent staining was performed as follows.[16] After deparaffinization and rehydration, tissue sections were blocked with a 2% bovine serum albumin (Sigma-Aldrich) and 0.1% Tween 20 (Sigma-Aldrich) solution for 1 h. Sections were then incubated for 1 h with a mouse anti-human CD-31 antibody (Dako), diluted 1:200 in a 0.1% Tween 20 solution. Sections were then washed four times for 1 min, followed by incubation for 1 h with an Alexa Fluor 488–labeled goat anti-mouse antibody (Invitrogen) diluted 1:500 in a 0.1% Tween 20 solution. Sections were washed four times for 1 min prior to imaging.

Statistical analysis

Average values are expressed as mean ± standard deviation. Differences between VD and FVD values were analyzed statistically using two-way analysis of variance (ANOVA) with repeated measures. Changes in FVD, VD, and FVD/VD values were analyzed statistically using the Mann–Whitney test. p-values < 0.05 were considered significant.

Results

Morphology of vessels in prevascularized tissues prior to implantation

The average vessel diameter over all portions of the prevascularized tissues prior to implantation was 11.9 ± 3.69 μm. The density of bifurcations was 220 ± 68.8 bifurcations/mm^2. The average vessel length between bifurcation nodes was 85 ± 40 μm.

Implanted prevascularized tissues anastomose with the host circulation

The prevascularized implants were largely transparent and thus facilitated imaging of both the implant itself and the underlying vasculature. Anastomosis between preformed vessels and the host circulation was easily detected by the presence of blood within the microvessels of the prevascularized tissue. Ten of the 12 prevascularized implants anastomosed with the host circulation as evidenced by the presence of blood within the implants. Anastomosis occurred an average of 3.5 ± 2.1 days following tissue implantation. Notably, the earliest time point at which anastomosis occurred was ~20 h. Figure 2 shows representative color images from both prevascularized and control tissues over 21 days. The presence of blood within the microvessels of the prevascularized tissue can be seen from day 7 onward (Fig. 2F–H). The presence of hemoglobin was detected and visualized with high contrast using hemoglobin absorption maps (Fig. 2I–L). Figure 2L reveals that perfused preformed vessels are present throughout the implant, but are more prominent in the periphery (Fig. 2G, H). No acellular control implant had any notable change aside from the gradual ingrowth of native vessels.

In all prevascularized tissues that anastomosed with the host circulation, extravasated blood was present at one or more locations and at multiple time points. Extravasated blood can be seen in Figure 2G and N (white arrows). Extravasated blood was resorbed in <3 days in all implants (Fig. 2H, O).

To confirm that the new blood-filled vessels such as those seen in Figure 2F–H were implanted human-derived vessels, and not the ingrowth of native vessels, ECFC-ECs embedded in two prevascularized tissues were stained with a lipophilic dye (DiO; Invitrogen) prior to implantation. Following anastomosis with the host circulation in these implants, fluorescence microscopy was used to confirm that the newly

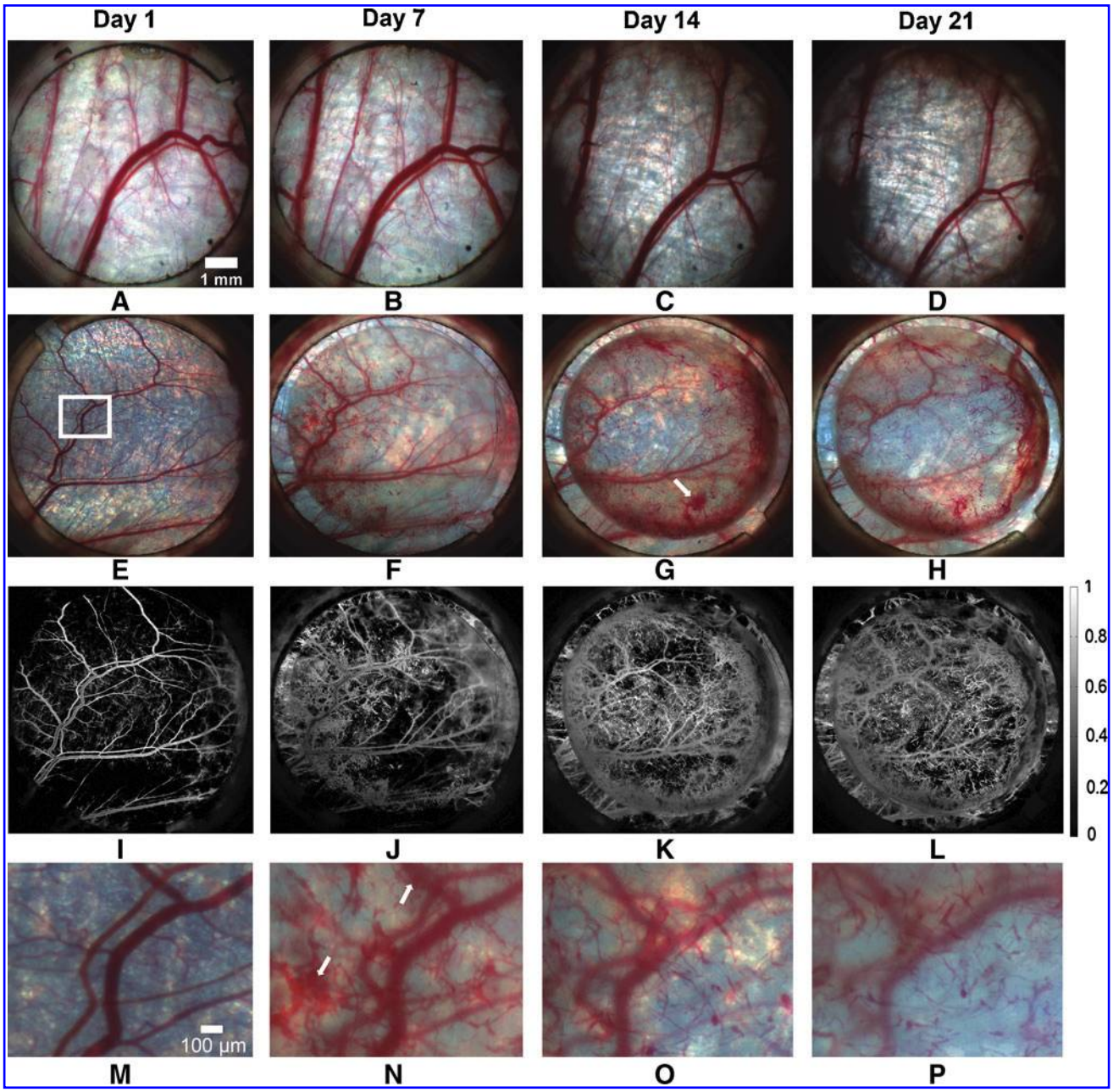

FIG. 2. MSI data allow visualization of implanted vessels perfused with blood from host vasculature following anastomosis. Perfused implanted vessels increased in number and are remodeled over the 21-day observation period. Color images of an acellular control implant **(A–D)** and a prevascularized implant **(E–H)** over a period of 21 days. **(I–L)** Hemoglobin absorption maps corresponding to **(E–H)**. **(M–P)** Magnified view of the region of interest highlighted in **(E)** over the same time period. White arrows indicate extravasated blood. Color images available online at www.liebertonline.com/tec

perfused vessels exhibited fluorescence consistent with the presence of DiO (Supplementary Fig. S1).

SO_2 maps reveal that prevascularized implants are initially perfused with oxygenated blood

All implanted human vessels that anastomosed with the host were filled with oxygenated blood (>90% hemoglobin saturation) within 24 h of initial anastomosis. The average hemoglobin oxygenation in the entire window chamber over time for control and prevascularized implants is presented in Figure 3A and B, respectively. Following the onset of anastomosis, a sharp increase in average hemoglobin oxygenation (days 1–5) was observed that resulted primarily from perfusion of preformed vessels with highly oxygenated blood. By day 5, the average hemoglobin oxygenation increased 53% over the initial value. This was followed by a decrease in hemoglobin oxygenation over the following three time points (Fig. 3C–E). SO_2 maps from day 21 were not used due to the natural regrowth of highly optically scattering fascial tissue within the window chamber that compromises measurement accuracy.

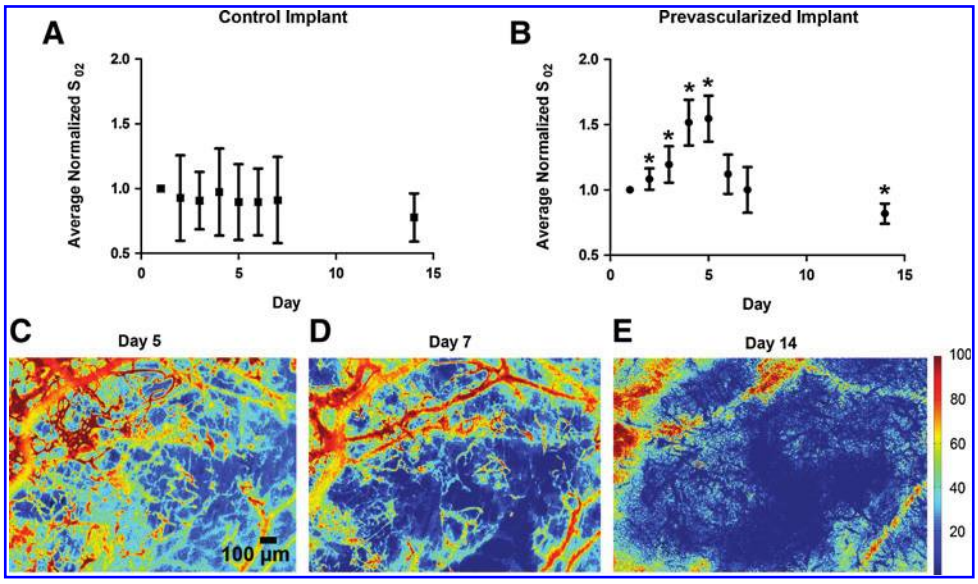

FIG. 3. Average hemoglobin oxygenation of prevascularized implants temporarily increases following anastomosis with the host. Plot of average normalized hemoglobin oxygenation values in entire window chamber for control **(A)** ($n=5$) and prevascularized implants **(B)** ($n=12$) over 14 days. Error bars represent standard deviation among mice at each time point. **(C–E)** Hemoglobin saturation maps of prevascularized tissue on day 5 **(C)**, day 7 **(D)**, and day 14 **(E)**, demonstrating progressive deoxygenation of preformed vessels. Units are percent hemoglobin oxygen saturation. Asterisk indicates significant ($p<0.05$ via Mann–Whitney test) change from day 1 value. Color images available online at www.liebertonline.com/tec

LSI and intravital microscopy reveal that blood flow within prevascularized implants does not persist

Figure 4A–E shows color images and corresponding SFI maps from a representative prevascularized tissue over 21 days. SFI values could be detected within prominent native vessels throughout all 21 days of imaging, demonstrating that blood flow was maintained throughout this period. In contrast, the LSI signal in preformed vessels was highly heterogeneous in space and time with most regions eliciting no signal. The presence of blood within vessels with no detectable SFI value is consistent with a lack of erythocyte movement, and thus a lack of flow. The absence of blood flow in the majority of preformed vessels was confirmed at higher magnification and with long exposure times ($T=1000$ ms; Fig. 4E2). These results were consistent across every exposure time used and were observed in every prevascularized tissue.

Plots of average FVD and FVD/VD (ratio of vessels exhibiting flow to total number of blood-filled vessels) are shown for both control and prevascularized tissues in Figure 5. Computed FVD/VD ratios do not approach 1 because the ability of LSI (used to compute FVD) to resolve blood vessels is less than that of MSI (used to compute VD). In the control tissues, FVD/VD did not change significantly over time, indicating that any new blood vessels were functional ($p\geq0.3939$ via Mann–Whitney test). Additionally, there was no significant difference between VD and FVD values ($p=0.9073$ via two-way ANOVA with repeated measures).

Conversely, VD increased over time in prevascularized implants due to the perfusion of preformed vessels. However, because the majority of preformed vessels did not exhibit continued flow, FVD values in these tissues did not rise concomitantly, resulting in a significant decrease in FVD/VD over time ($p\leq0.0079$ via Mann–Whitney test). Unlike the control implants, the difference between VD and FVD was significant in prevascularized tissues ($p<0.0001$ via two-way ANOVA with repeated measures).

To confirm that flow ceases within preformed vessels, FITC-dextran was injected retro-orbitally into three mice following anastomosis to assess whether the fluorophore flowed into the prevascularized implant. Each of the three mice was imaged at a different time point following initial anastomosis—<1 h, 3 days, and 5 days—to determine when thrombosis occurs. The results are shown in Figure 6.

Figure 6A and B shows the border between native tissue and implanted tissue that was initially perfused 5 days earlier. The PDMS-retaining ring was removed prior to tissue implantation to achieve this interface. Figure 6A shows that preformed vessels anastomose with native blood vessels of similar cailber, which can be assumed to be capillaries based on their size and morphology. Figure 6A also shows that blood is present within the preformed vessels of the prevascularized implants due to perfusion at an earlier time point; however, visualizing the same region using fluorescent microscopy indicates that the fluorescent dextran did not flow into the prevacualrized tissue (Fig. 6B). Fluorescent signal visible within the prevascularized implant in Figure 6B originates from fluorescence of the native vasculature underlying the implant. Lack of flow into the prevascularized tissue persisted up to 40 min, after which imaging was ceased. Similar results were seen in the mouse imaged 3 days after preformed vessel perfusion.

Figure 6C–G shows fluorescence images acquired from implanted vessels that underwent intial perfusion <1 h before imaging. Figure 6C–F shows implanted vessels filled with intraluminal mouse erythrocytes (white arrows). These images were taken with 2 s between each acquisition and

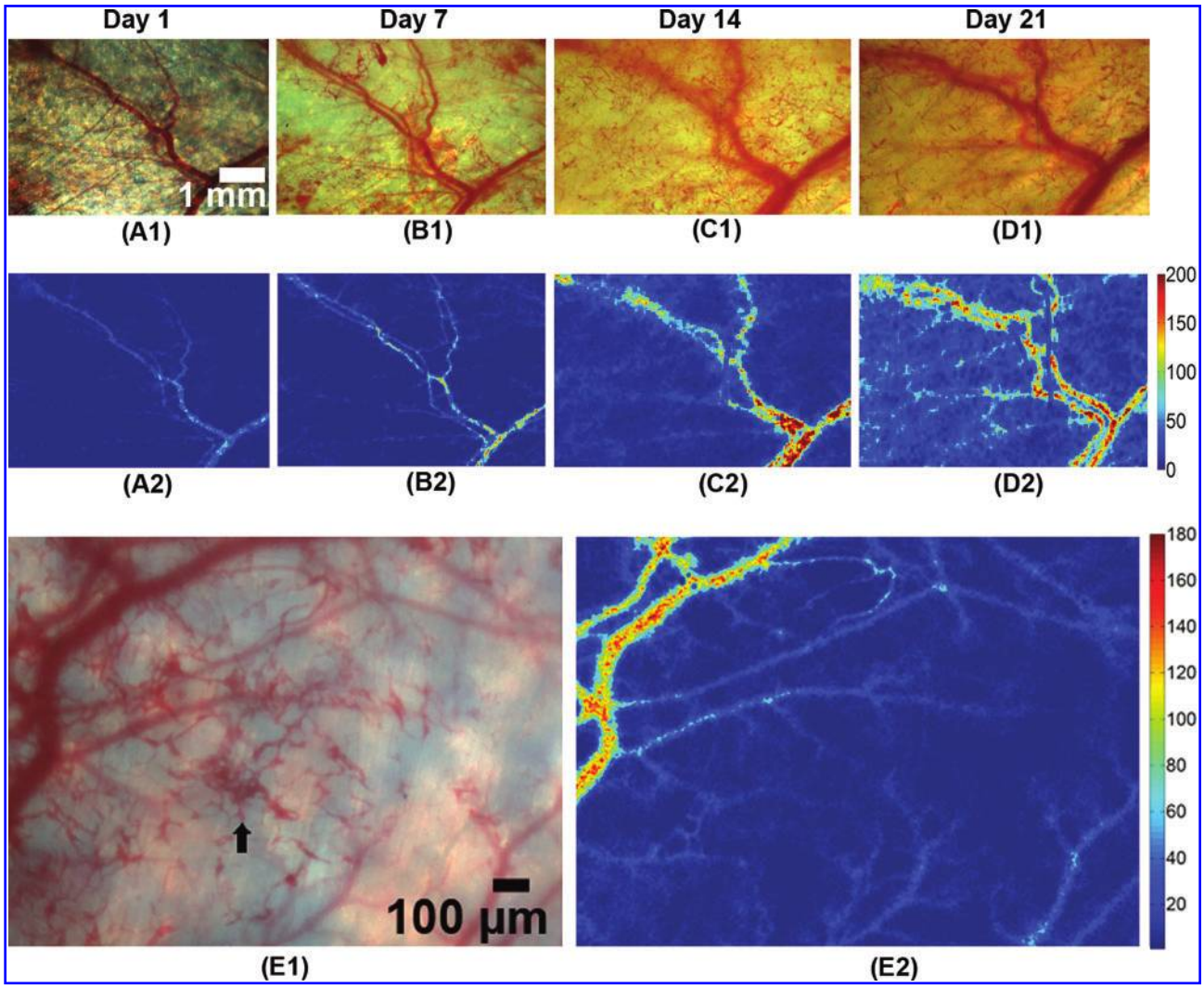

FIG. 4. LSI data show that flow does not persist in the majority of blood-filled preformed vessels. **(A1–D1)** Color images and corresponding speckle flow index (SFI) maps **(A2–D2)** acquired using LSI of prevascularized implant on days 1, 7, 14, and 21. **(E1)** Color image of perfused preformed vessels and underlying native vessels on day 7. Blood-filled preformed vessels can be identified by their small diameter and characteristic tortuous morphology (black arrow). **(E2)** SFI map with $T = 1000$ ms corresponding to **(E1)** showing that flow is present in native vessels but absent in previously perfused implanted vessels. Unit is s^{-1}. Color images available online at www.liebertonline.com/tec

demonstrate the flow of erythrocytes (see Supplementary Video S1). This timecourse was started 30 min post-FITC-dextran injection. Figure 6G was acquired 10 min after Figure 6C–F and shows that flow has ceased due to clot formation (white arrow).

The computed wall shear rates within four preformed vessels in and around Figure 6C–G were 37, 16, 29, and $3.2\,s^{-1}$, giving an average of $21 \pm 15\,s^{-1}$. The vessels with wall shear rates of 3.2 and $16\,s^{-1}$ are indicated by red and yellow arrows in Figure 6D, respectively. Native vessels proximal but not seen in Figure 6 were found to have significantly higher wall shear rates—374, 490, and $402\,s^{-1}$, giving an average of $422 \pm 61\,s^{-1}$.

Histology may not provide evidence of thrombosis

Histological analysis of excised tissues showed many implanted human-derived vessels that had been perfused with host blood as evidenced by the presence of erythrocytes. Such vessels were identified by finding intraluminal erythrocytes in hematoxylin and eosin–stained slides followed by identifying the vessels in adjacent sections and confirming that they were labeled with anti-human CD-31. Significantly, many implanted vessels that were shown previously to be nonfunctional lacked clear evidence of intraluminal thrombi under histological analysis (Supplementary Fig. S2).

Discussion

Perhaps the most prominent obstacle limiting the creation of engineered tissue that mimics the size and function of complex native tissue is adequate delivery of oxygen following implantation. Several strategies have been employed to overcome this limitation, all of which are aimed at quickly and permanently vascularizing implanted engineered tissues. However, regardless of the strategy employed, it is

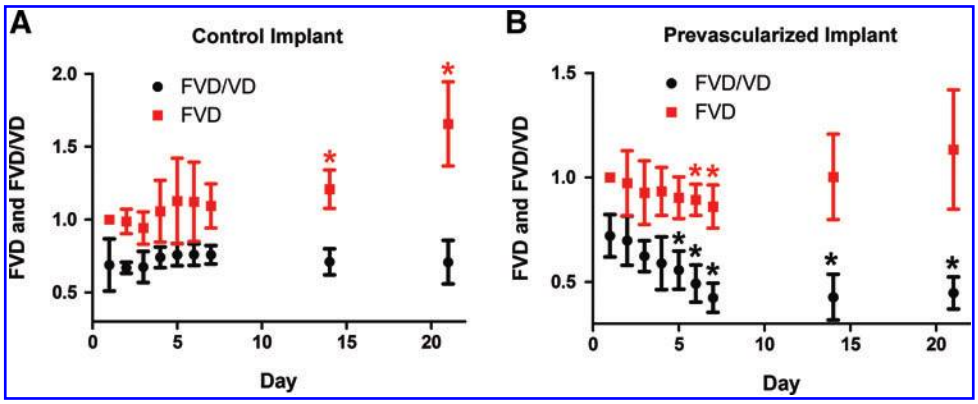

FIG. 5. Lack of flow in implanted vessels following initial perfusion results in a significant decrease in the ratio of functional vessels to nonfunctional vessels (functional vascular density/vascular density [FVD/VD]). Plots of FVD and FVD/VD for control **(A)** ($n=5$) and prevascularized implants **(B)** ($n=12$). Ingrowth of only functional vessels in control implants results in a significant increase in VD, but insignificant change in FVD/VD over time. In prevascularized tissues, perfusion followed by thrombosis in implanted vessels results in significant increase in VD without proportional increase in FVD. As a result, FVD/VD decreases significantly over time. Error bars represent standard deviation among mice at each time point. Asterisk indicates significant ($p<0.05$ via Mann–Whitney test) change from day 1 value. Color images available online at www.liebertonline.com/tec

critical to assess blood flow, oxygenation, and vessel morphology of the implanted engineered tissues dynamically (i.e., across multiple time points) to facilitate their appropriate design. To this end, we have developed noninvasive optical imaging methods capable of assessing the blood flow and oxygenation in an implantable tissue. Our results in a prevascularized fibrin-based tissue demonstrate early anastomosis and oxygenation, but little-to-no flow, which could compromise cell viability in more complex tissues.

A variety of intravital imaging techniques have been used previously to analyze tissue or cells implanted into small rodents. Multiphoton microscopy has been used by Koike

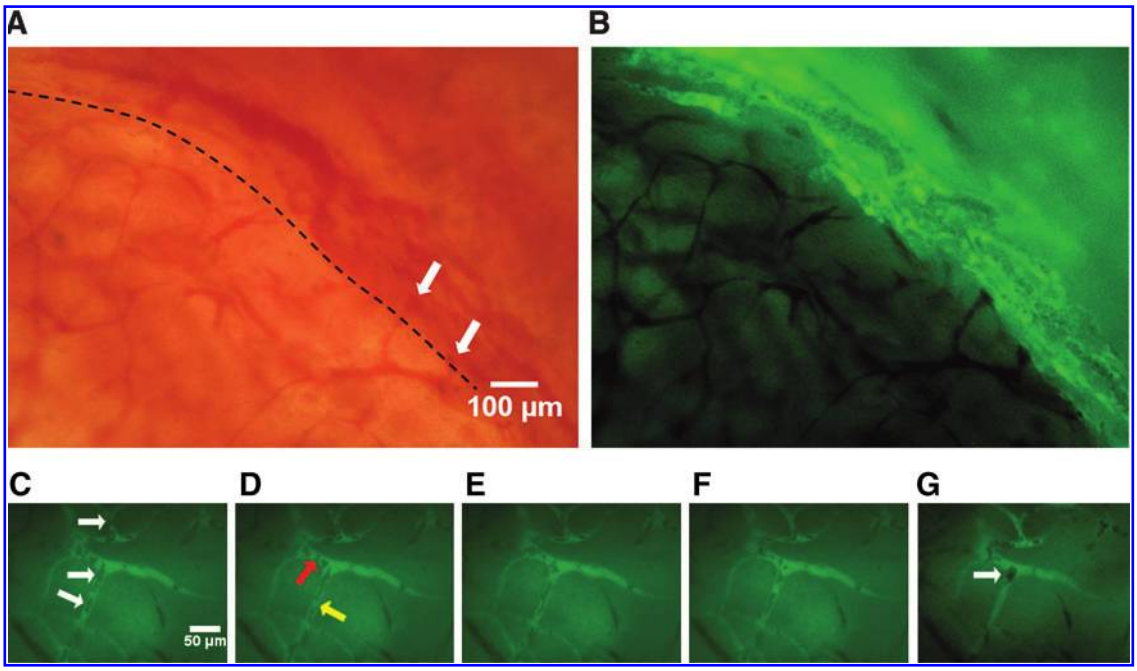

FIG. 6. Host blood initially perfuses implanted vessels; however, the formation of thrombi prevents continued flow within these vessels. **(A)** Color image of border between prevascularized implant (below black-dotted line) and native tissue (above black-dotted line). White arrows indicate regions of anastomosis. **(B)** Fluorescence image of region in **(A)** indicating that no fluorescent dextran can flow into the prevascularized tissue. **(A)** and **(B)** were acquired 5 days following initial implanted vessel perfusion. **(C–G)** Fluorescent images acquired 30 **(C–F)** and 40 **(G)** min post-fluorescein isothiocyanate–dextran injection. There is a 2 s delay between each image **(C–F)**. **(C)** Shows flowing mouse erythrocytes (white arrows). **(D)** Shows two preformed vessels where wall shear rate was computed (red arrow $=3.2\,s^{-1}$, yellow arrow $=16\,s^{-1}$). **(G)** Shows the formation of thrombus (white arrow) that induced flow cessation. **(C–G)** were acquired <1 h following initial implanted vessel perfusion. Color images available online at www.liebertonline.com/tec

et al.[24] to longitudinally analyze the structure and function of blood vessels derived from human umbilical vein endothelial cells (HUVECs) implanted into mice bearing cranial window chambers. A similar study by Au *et al*.[26] also used multiphoton microscopy to study the potential of peripheral and umbilical cord blood–derived endothelial progenitor cells (here referred to as ECFC-ECs[41]) to form functional, long-lasting blood vessels. Multiphoton microscopy has also been used to acquire blood flow velocity maps in cranial window chambers.[42,43] One disadvantage of this technique is the need for scanning of the excitation source, thus limiting temporal resolution. This drawback has been avoided by using fluorescence microscopy and MSI to study implanted tissue. Laschke *et al*.[13] used fluorescence microscopy to study remodeling and blood flow in poly-lactic-glycolic acid–based implants prevascularized *in situ* and implanted into a mouse dorsal window chamber. Sorg *et al*.[25] used MSI to assess vascularization and oxygenation of 4T1 mouse mammary carcinoma spheroids implanted into a mouse dorsal window chamber.

Several other imaging techniques have been used to acquire functional information from a larger field of view than that provided by microscopy. These include bioluminescent imaging performed using whole small rodent imaging systems. This technique has been used to quantitatively assess oxygenation, perfusion, and survival in implanted engineered skeletal muscle tissue and Chinese hamster ovary cells.[14,44] Additionally, the morphology of implanted engineered tissue has also been analyzed using magnetic resonance imaging (MRI) and micro-computed tomography (micro-CT) with exogenous contrast agents.[45–47]

While the just outlined microscopy techniques provide excellent contrast and spatial resolution, the imaging field of view is generally limited to hundreds of micrometers, making use of this technique impractical for the study of millimeter-scale implanted tissue. Additionally, bioluminescent imaging requires the use of transgenic cells capable of oxidizing a substrate that must be injected before imaging as well as reach the enzyme through the circulation. The latter is clearly a problem when the goal is to assess the perfusion adequacy of a vascular network. Finally, MRI and micro-CT have very limited temporal resolution, are relatively expensive, have spatial resolution less than microscopy, and, in the case of micro-CT, uses potentially harmful ionizing radiation.[48]

This study therefore utilized full-field MSI and LSI, allowing us to assess the dynamics of vascular remodeling, blood flow, and hemoglobin oxygen saturation in implanted engineered tissues at relatively large length scales, and without the need of a substrate–enzyme reaction. The use of intravital fluorescence microscopy in addition to these techniques allowed the assessment of blood flow with high temporal (30 frames/s) and spatial resolution. Further, region of interest selection during intravital microcopy could be guided by full-field MSI and LSI data. Used together, these imaging techniques provide previously unavailable information integral to understanding the dynamic changes within millimeter-scale implantable tissues.

Anastomosis with host circulation

In this study, prevascularized tissues were nearly transparent upon implantation into the window chamber. As a result, areas of anastomosis between the preformed microvessel network and the host circulation were easily identified by the presence of blood within the tissue in color images or hemoglobin absorption maps. A large variation in the time required for anastomosis between the implanted tissues and host vasculature was observed ($\sim$20 h to 7 days). Additionally, two of the implants did not anastomose with the host vasculature after 21 days of observation. This variability is potentially due to donor variability and small differences in passage number in the ECFC-ECs used in this study, as these factors have been shown to significantly affect the proliferation rate of ECFC-ECs.[49,50] A slower rate of ECFC-EC proliferation and thus vessel growth would likely extend the time required for anastomosis between the implant and host vasculature.

All prevascularized tissues that anastomosed with the host circulation demonstrated that areas of initial perfusion were at first isolated. Over a period of several days, the number and size of individual regions of perfused preformed vessels increased. This suggests that single anastomosis was inadequate for perfusion of the entire vascular network, despite preformed vessels being present throughout the tissue as confirmed by *in vitro* CD-31 staining (data not shown).

Blood extravasation and localization in implanted vessels

In many of the prevascularized tissues, blood within the implant initially appeared diffuse and was not highly localized within preformed vessels (Fig. 2G, N), but rather within the matrix itself. Over a period of 1–3 days, diffuse blood within the matrix was removed and vessels with intraluminal blood became visible. Removal of extravasated blood and subsequent changes in vessel morphology are consistent with erythrocyte resorption and vessel remodeling.

One possible mechanism by which this sequence of events occurs is that upon anastomosis with the host circulation, blood entering preformed vessels may extravasate due to the relative immaturity of the vascular network. It has been shown that pericyte-like coverage of these blood vessels by the NHLFs is limited,[16] and thus vessel stabilization is likely incomplete, possibly leading to excessive vascular permeability.[51] The hemorrhaging could then potentially elicit the closing of vessel wall gaps via expression of protease-activated G protein–coupled receptor 1 by endothelial cells.[52]

Hemoglobin oxygen saturation

SO_2 maps were effective for monitoring the hemoglobin saturation both in blood-filled preformed vessels, as well as in the underlying native vasculature. Our result that many blood-filled preformed vessels reached oxygen saturation levels of $\sim$0% despite being located at a distance of $<$200 μm (the diffusion path length of oxygen in highly cellularized tissue[1–3]) from a native arteriole may indicate that the intraluminal hemoglobin had become denatured and thus lost its oxygen-carrying capacity.

Nonetheless, our results demonstrate that early anastomosis with a microvessel network developed *in vitro* can provide oxygenated hemoglobin to a thick tissue for a short period of time. This amount of time may provide enough oxygen to maintain cell viability and tissue function while

native vessels invade the implantable tissue, providing a long-term solution to oxygen delivery. The average normalized SO_2 value for the prevascularized implant was significantly lower on day 14 than its baseline value on day 1. This is due to the fact that deoxygenated preformed vessels began to occasionally mask native oxygenated vessel during imaging, as seen in Figure 3E. As a result, the computed average normalized SO_2 value was erroneously decreased to a small degree.

It should additionally be noted that SO_2 mapping was performed while mice were anesthetized with 1.5% isoflurane and balance oxygen. This very likely resulted in elevated blood oxygenation levels as well as vascular morphological changes because isoflurane has been shown to induce vasodilation.[53] However, it is interesting to note that blood-filled preformed vessels deoxygenated even under these circumstances.

Flow and thrombosis following anastomosis

LSI and intravital microscopy were found to be very effective for monitoring blood flow in both native and preformed vasculature. Although the functionality of prevascularized implant vasculature has been assessed *in vivo* via imaging previously, no previous work has been able to provide both microscopic and full-field visualization of flow and hemoglobin saturation.[13,14,24] These techniques demonstrated that following initial perfusion, virtually no blood flow was maintained in preformed vessels after 2 h due to thrombus formation as seen in Figure 6G.

The formation of thrombi may be attributed to preformed vessels that exhibit lumen diameters that are too small to conduct erythrocytes, and thus induce the cessation of flow. However, even preformed vessels with lumen diameters $<7\,\mu m$ were filled with blood as seen in Figures 6A and 4E1. A more significant source of thrombosis is likely the presence of low shear rates within preformed vessels since blood vessels exhibiting low shear and flow are predisposed to thrombus formation.[54] Specifically, it has been shown that shear rates of less than $\sim 100\,s^{-1}$ in vessels may result in longer residence times of clotting factors, thus promoting the initiation of blood coagulation.[55] In addition, blood exhibits shear thinning (increase in viscosity) due to the deformation and aggregation of erythrocytes for shear rates less than $\sim 100\,s^{-1}$.[56,57] It was found that the wall shear rates in the preformed vessels in Figure 6C–G were below this threshold with an average shear rate of $21 \pm 15\,s^{-1}$. In contrast, the closest three native vessels of comparable caliber ($\sim$10-μm diameter) had an average shear rate of $422 \pm 61\,s^{-1}$. The preformed vessel with the lowest shear rate, $3.2\,s^{-1}$, was the first of the observed vessels in which a thrombus formed.

The rationale for the low shear rates observed in preformed vessels can be explained as follows. Native blood vessels typically follow Murray's law at bifurcations, resulting in the conservation of shear rate.[58] Shear rates in all vessels, therefore, only vary from ~ 100 to $\sim 1000\,s^{-1}$ under normal conditions.[55] Conversely, *in vitro* inspection of bifurcating preformed vessels demonstrates that parent vessels have approximately the same diameter as the daughter vessels—a violation of Murray's law. If the volumetric flow in daughter vessels is assumed to be equal, shear rate will be halved in preformed vessels at each bifurcation.

It was found that preformed vessels anastomose with nearby native capillaries, which were found to have an average shear rate of $422\,s^{-1}$. If this shear rate is assumed at the point of anastomosis between the host vasculature and preformed vessels, shear rate will be halved at each bifurcation and will fall below the predicted threshold for thrombus formation ($100\,s^{-1}$) after only three bifurcations. Given that the average number of vessel bifurcations in the prevascularized tissues used in this experiment was 220 bifurcations/mm^2, it can be estimated that a prevascularized tissue with an area of only 9.1×10^{-3} mm^2 could remain functional following anastomosis with the host. Larger prevascularized tissues could be supported if the number of bifurcations is reduced. Alternatively, anticoagulants administered to implant hosts may prevent thrombus formation long enough for the vascular remodeling necessary to achieve higher shear rates within preformed vessels to occur. This will be the focus of future studies.

Functional imaging provides critical information unavailable using histology

It is common for histology to be used as a means of determining whether perfusion of implanted prevascularized tissues has occurred based upon the presence of host blood within the implanted tissue.[15,16,19–23] The use of histology to analyze the prevascularized tissues in this study showed the presence of mouse erythrocytes within preformed vessels (Supplementary Fig. S2). However, many histological sections erroneously suggested continued flow within implanted vessels as intraluminal erythrocytes could be seen without the presence of blood clot. Thus, functional imaging was necessary to observe that FVD did not increase concomitantly with VD in prevascularized tissues. Further, use of histology would not have provided information regarding the progressive deoxygenation of preformed vessels, emphasizing that such methods are inadequate for studying the hemodynamics and thus viability and function of implanted engineered tissues.

Summary

LSI, MSI, and intravital microscopy were used to analyze blood flow and hemoglobin saturation in implanted prevascularized tissues. We found that perfusion with oxygenated blood occurs in prevascularized tissues following anastomosis with the host circulation in <20 h following implantation, but that flow did not persist due to thrombus formation. Thrombosis may result from shear rates in preformed vessels dropping below a critical threshold ($\sim 100\,s^{-1}$) for blood coagulation. Limiting the scale or degree of vascular interconnectivity in prevascularized tissues may overcome this problem. Nonetheless, the observed transient increase in SO_2 may maintain implant viability long enough for remodeling or vascularization to occur. Finally, identifying erythrocytes within prevascularized tissues via histological analysis is not necessarily consistent with continuous blood flow and oxygen delivery, which were found to change dynamically. These changes highlight that histology is inappropriate for characterizing such implants and emphasize the need to acquire dynamic imaging information to better understand host–implant interactions.

Sources of Funding

This work was supported in part by the Arnold and Mabel Beckman Foundation (B.C.), the National Science Foundation through a Graduate Research Fellowship to Sean White, a Dean's Triumvirate Grant from the UC-Irvine College of Health Sciences (B.C., S.C.G., and C.C.W.H.), grants from the National Heart Lung and Blood Institute (R21 HL104203, S.C.G. and C.C.W.H.), and the National Institutes of Health Laser Microbeam and Medical Program (LAMMP, a P41 Technology Research Resource, B.C.).

Disclosure Statement

No competing financial interests exist.

References

1. Carmeliet, P., and Jain, R.K. Angiogenesis in cancer and other diseases. Nature **407,** 249, 2000.
2. Muschler, G.F., Nakamoto, C., and Griffith, L.G. Engineering principles of clinical cell-based tissue engineering. J Bone Joint Surg Am **86,** 1541, 2004.
3. Helmlinger, G., Yuan, F., Dellian, M., and Jain, R.K. Interstitial pH and pO2 gradients in solid tumors *in vivo*: high-resolution measurements reveal a lack of correlation. Nat Med **3,** 177, 1997.
4. Liu, P., Deng, Z., Han, S., Liu, T., Wen, N., Lu, W., Geng, X., Huang, S., and Jin, Y. Tissue-engineered skin containing mesenchymal stem cells improves burn wounds. Artif Organs **32,** 925, 2008.
5. Nie, X., Cai, J.K., Yang, H.M., Xiao, H.A., Wang, J.H., Wen, N., Zhang, Y.J., and Jin, Y. Successful application of tissue-engineered skin to refractory ulcers. Clin Exp Dermatol **32,** 699, 2007.
6. Fujihara, Y., Asawa, Y., Takato, T., and Hoshi, K. Tissue reactions to engineered cartilage based on poly-L-lactic acid scaffolds. Tissue Eng Part A **15,** 1565, 2008.
7. Hunziker, E.B. Articular cartilage repair: basic science and clinical progress. A review of the current status and prospects. Osteoarthritis Cartilage **10,** 432, 2002.
8. Pei, M., He, F., Boyce, B.M., and Kish, V.L. Repair of full-thickness femoral condyle cartilage defects using allogeneic synovial cell-engineered tissue constructs. Osteoarthritis Cartilage **17,** 714, 2009.
9. Ryu, W., Min, S.W., Hammerick, K.E., Vyakarnam, M., Greco, R.S., Prinz, F.B., and Fasching, R.J. The construction of three-dimensional micro-fluidic scaffolds of biodegradable polymers by solvent vapor based bonding of micromolded layers. Biomaterials **28,** 1174, 2007.
10. Richardson, T.P., Peters, M.C., Ennett, A.B., and Mooney, D.J. Polymeric system for dual growth factor delivery. Nat Biotech **19,** 1029, 2001.
11. Ott, H.C., Matthiesen, T.S., Goh, S.-K., Black, L.D., Kren, S.M., Netoff, T.I., and Taylor, D.A. Perfusion-decellularized matrix: using nature's platform to engineer a bioartificial heart. Nat Med **14,** 213, 2008.
12. Gilbert, T.W., Sellaro, T.L., and Badylak, S.F. Decellularization of tissues and organs. Biomaterials **27,** 3675, 2006.
13. Laschke, M.W., Rücker, M., Jensen, G., Carvalho, C., Mülhaupt, R., Gellrich, N.-C., and Menger, M.D. Improvement of vascularization of PLGA scaffolds by inosculation of in situ-preformed functional blood vessels with the host microvasculature. Ann Surg **248,** 939, 2008.
14. Levenberg, S., Rouwkema, J., Macdonald, M., Garfein, E.S., Kohane, D.S., Darland, D.C., Marini, R., Van Blitterswijk, C.A., Mulligan, R.C., D'amore, P.A., and Langer, R. Engineering vascularized skeletal muscle tissue. Nat Biotech **23,** 879, 2005.
15. Chen, X., Aledia, A.S., Ghajar, C.M., Griffith, C.K., Putnam, A.J., Hughes, C.C.W., and George, S.C. Prevascularization of a fibrin-based tissue construct accelerates the formation of functional anastomosis with host vasculature. Tissue Eng Part A **15,** 1363, 2008.
16. Chen, X., Aledia, A.S., Popson, S.A., Him, L., Hughes, C.C.W., and George, S.C. Rapid anastomosis of endothelial progenitor cell–derived vessels with host vasculature is promoted by a high density of cotransplanted fibroblasts. Tissue Eng Part A **16,** 585, 2010.
17. Clark, E.R., and Clark, E.L. Microscopic observations on the growth of blood capillaries in the living mammal. Am J Anat **64,** 251, 1939.
18. Rouwkema, J., Rivron, N.C., and Van Blitterswijk, C.A. Vascularization in tissue engineering. Trends Biotechnol **26,** 434, 2008.
19. Rouwkema, J., Westerweel, P.E., Boer, J.D., Verhaar, M.C., and Van Blitterswijk, C.A. The use of endothelial progenitor cells for prevascularized bone tissue engineering. Tissue Eng Part A **15,** 2015, 2009.
20. Verseijden, F., Posthumus-Van Sluijs, S.J., Van Neck, J.W., Hofer, S.O.P., Hovius, S.E.R., and Van Osch, G.J.V.M. Vascularization of prevascularized and non-prevascularized fibrin-based human adipose tissue constructs after implantation in nude mice. J Tissue Eng Regen Med **6,** 169, 2012.
21. Dvir, T., Kedem, A., Ruvinov, E., Levy, O., Freeman, I., Landa, N., Holbova, R., Feinberg, M.S., Dror, S., Etzion, Y., Leor, J., and Cohen, S. Prevascularization of cardiac patch on the omentum improves its therapeutic outcome. Proc Natl Acad Sci U S A **106,** 14990, 2009.
22. Unger, R.E., Ghanaati, S., Orth, C., Sartoris, A., Barbeck, M., Halstenberg, S., Motta, A., Migliaresi, C., and Kirkpatrick, C.J. The rapid anastomosis between prevascularized networks on silk fibroin scaffolds generated *in vitro* with cocultures of human microvascular endothelial and osteoblast cells and the host vasculature. Biomaterials **31,** 6959, 2010.
23. Nör, J.E., Peters, M.C., Christensen, J.B., Sutorik, M.M., Linn, S., Khan, M.K., Addison, C.L., Mooney, D.J., and Polverini, P.J. Engineering and characterization of functional human microvessels in immunodeficient mice. Lab Invest **81,** 453, 2001.
24. Koike, N., Fukumura, D., Gralla, O., Au, P., Schechner, J.S., and Jain, R.K. Tissue engineering: creation of long-lasting blood vessels. Nature **428,** 138, 2004.
25. Sorg, B.S., Moeller, B.J., Donovan, O., Cao, Y., and Dewhirst, M.W. Hyperspectral imaging of hemoglobin saturation in tumor microvasculature and tumor hypoxia development. J Biomed Opt **10,** 44004, 2005.
26. Au, P., Daheron, L.M., Duda, D.G., Cohen, K.S., Tyrrell, J.A., Lanning, R.M., Fukumura, D., Scadden, D.T., and Jain, R.K. Differential *in vivo* potential of endothelial progenitor cells from human umbilical cord blood and adult peripheral blood to form functional long-lasting vessels. Blood **111,** 1302, 2008.
27. Boas, D.A., and Dunn, A.K. Laser speckle contrast imaging in biomedical optics. J Biomed Opt **15,** 011109, 2010.
28. Choi, B., Kang, N.M., and Nelson, J.S. Laser speckle imaging for monitoring blood flow dynamics in the *in vivo* rodent dorsal skin fold model. Microvasc Res **68,** 143, 2004.

29. Choi, B., Ramirez-San-Juan, J.C., Lotfi, J., and Nelson, J.S. Linear response range characterization and *in vivo* application of laser speckle imaging of blood flow dynamics. J Biomed Opt **11,** 041129, 2006.
30. Dunn, A.K., Bolay, H., Moskowitz, M.A., and Boas, D.A. Dynamic imaging of cerebral blood flow using laser speckle. J Cereb Blood Flow Metab **21,** 195, 2001.
31. Papenfuss, H.D., Gross, J.F., Intaglietta, M., and Treese, F.A. A transparent access chamber for the rat dorsal skin fold. Microvasc Res **18,** 311, 1979.
32. Moy, A., White, S., Indrawan, E., Lotfi, J., Nudelman, M., Costantini, S., Agarwal, N., Jia, W., Kelly, K., Sorg, B., and Choi, B. Wide-field functional imaging of blood flow and hemoglobin oxygen saturation in the rodent dorsal window chamber. Microvasc Res **82,** 199, 2011.
33. Bui, A.K., Teves, K.M., Indrawan, E., Jia, W., and Choi, B. Longitudinal, multimodal functional imaging of microvascular response to photothermal therapy. Opt Lett **35,** 3216, 2010.
34. Fercher, A.F., and Briers, J.D. Flow visualization by means of single-exposure speckle photography. Opt Commun **37,** 326, 1981.
35. Yuan, S., Devor, A., Boas, D.A., and Dunn, A.K. Determination of optimal exposure time for imaging of blood flow changes with laser speckle contrast imaging. Appl Optics **44,** 1823, 2005.
36. White, S.M., George, S.C., and Choi, B. Automated computation of functional vascular density using laser speckle imaging in a rodent window chamber model. Microvasc Res **82,** 92, 2011.
37. Kirkpatrick, S.J., Duncan, D.D., and Wells-Gray, E.M. Detrimental effects of speckle-pixel size matching in laser speckle contrast imaging. J Biomed Opt **33,** 2886, 2008.
38. Ramirez-San-Juan, J.C., Ramos-García, R., Guizar-Iturbide, I., Martínez-Niconoff, G., and Choi, B. Impact of velocity distribution assumption on simplified laser speckle imaging equation. Opt Express **16,** 3197, 2008.
39. Shonat, R.D., Wachman, E.S., Niu, W., Koretsky, A.P., and Farkas, D.L. Near-simultaneous hemoglobin saturation and oxygen tension maps in mouse brain using an AOTF microscope. Biophys J **73,** 1223, 1997.
40. Roggan, A., Friebel, M., Dörschel, K., Hahn, A., and Müller, G. Optical properties of circulating human blood in the wavelength range 400–2500 nm. J Biomed Opt **4,** 1999.
41. Yoder, M.C., Mead, L.E., Prater, D., Krier, T.R., Mroueh, K.N., Li, F., Krasich, R., Temm, C.J., Prchal, J.T., and Ingram, D.A. Redefining endothelial progenitor cells via clonal analysis and hematopoietic stem/progenitor cell principals. Blood **109,** 2007.
42. Schaffer, C.B., Friedman, B., Nishimura, N., Schroeder, L.F., Tsai, P.S., Ebner, F.F., Lyden, P.D., and Kleinfeld, D. Two-photon imaging of cortical surface microvessels reveals a robust redistribution in blood flow after vascular occlusion. PLoS Biol **4,** 258, 2006.
43. Kamoun, W.S., Chae, S.-S., Lacorre, D.A., Tyrrell, J.A., Mitre, M., Gillissen, M.A., Fukumura, D., Jain, R.K., and Munn, L.L. Simultaneous measurement of RBC velocity, flux, hematocrit and shear rate in vascular networks. Nat Meth **7,** 655, 2010.
44. Liu, J., Barradas, A., Fernandes, H., Janssen, F., Papenburg, B., Stamatialis, D., Martens, A., Blitterswijk, C.V., and Boer, J.D. In vitro and in vivo bioluminescent imaging of hypoxia in tissue-engineered grafts. Tissue Eng Part C **16,** 479, 2010.
45. Appel, A., Anastasio, M.A., and Brey, E.M. Potential for imaging engineered tissues with X-ray phase contrast. Tissue Eng Part B **17,** 321, 2011.
46. Zimmermann, W.-H., Melnychenko, I., Wasmeier, G., Didie, M., Naito, H., Nixdorff, U., Hess, A., Budinsky, L., Brune, K., Michaelis, B., Dhein, S., Schwoerer, A., Ehmke, H., and Eschenhagen, T. Engineered heart tissue grafts improve systolic and diastolic function in infarcted rat hearts. Nat Med **12,** 452, 2006.
47. Faraj, K.A., Cuijpers, V.M.J.I., Wismans, R.G., Walboomers, X.F., John A. Jansen, Kuppevelt, T.H.V., and Daamen, W.F. Micro-computed tomographical imaging of soft biological materials using contrast techniques. Tissue Eng Part C **15,** 493, 2009.
48. Mcdonald, D.M., and Choyke, P.L. Imaging of angiogenesis: from microscope to clinic. Nat Med **9,** 713, 2003.
49. Melero-Martin, J.M., Khan, Z.A., Picard, A., Wu, X., Paruchuri, S., and Bischoff, J. *In vivo* vasculogenic potential of human blood-derived endothelial progenitor cells. Blood **109,** 4761, 2007.
50. Ingram, D.A., Caplice, N.M., and Yoder, M.C. Unresolved questions, changing definitions, and novel paradigms for defining endothelial progenitor cells. Blood **106,** 1525, 2005.
51. Benjamin, L.E., Hemo, I., and Keshet, E. A plasticity window for blood vessel remodelling is defined by pericyte coverage of the preformed endothelial network and is regulated by PDGF-B and VEGF. Development **125,** 1591, 1998.
52. Carmeliet, P. Clotting factors build blood vessels. Science **293,** 1602, 2001.
53. Schwinn, D.A., Mcintyre, R.W., and Reves, J.G. Isoflurane-induced vasodilation. Anesth Analg **71,** 451, 1990.
54. Farb, A., Burke, A.P., Kolodgie, F.D., and Virmani, R. Pathological mechanisms of fatal late coronary stent thrombosis in humans. Circulation **108,** 1701, 2003.
55. Shen, F., Kastrup, C.J., Liu, Y., and Ismagilov, R.F. Threshold response of initiation of blood coagulation by tissue factor in patterned microfluidic capillaries is controlled by shear rate. Arterioscl Throm Vas **28,** 2035, 2008.
56. Eckmann, D.M., Bowers, S., Stecker, M., and Cheung, A.T. Hematocrit, volume expander, temperature, and shear rate effects on blood viscosity. Anesth Analg **91,** 539, 2000.
57. Chien, S. Shear dependence of effective cell volume as a determinant of blood viscosity. Science **168,** 977, 1970.
58. Murray, C.D. The physiological principle of minimum work. I. The vascular system and the cost of blood volume. Proc Natl Acad Sci U S A **12,** 207, 1926.

Address correspondence to:
Bernard Choi, Ph.D.
Department of Biomedical Engineering
University of California
1002 Health Sciences Road E
University of California
Irvine, CA 92697

E-mail: choib@uci.edu

Received: December 30, 2011
Accepted: March 14, 2012
Online Publication Date: May 16, 2012